AIAA JOURNAL
Vol. 47, No. 10, October 2009

Prebuckling and Buckling of Unsymmetrically Laminated Composite Panels with Stringer Run-Outs

Enzo Cosentino*
Airbus Operations, Ltd., Bristol, England BS34 7AR, United Kingdom
and
Paul Weaver†
University of Bristol, Bristol, England BS8 1TR, United Kingdom

DOI: 10.2514/1.44665

A meshless approach is developed and used to predict buckling loads of discretely assembled composite panels made from skin and stiffeners. Particular emphasis is given to stringer run-outs within a stiffened panel, where abrupt eccentricity can trigger very large transverse displacements of the skin in front of the run-out tip and perturb the internal in-plane loads distribution. The effect of load eccentricity is included in the formulation. The final set of nonlinear equations is obtained by combining von Kármán's formulation for moderately large deflections in plates with an extended Timoshenko approach for small initial perturbations. Solutions are calculated by means of a Rayleigh–Ritz method in conjunction with a Galerkin technique. Orthogonal eigenfunctions are employed to expand the variables of interest in generalized Fourier series. An iterative algorithm is proposed to calculate buckling loads. Limits of applicability, convergence of results, and further potential exploitations are discussed. Numerical results are compared with those from finite element analysis and other numerical approaches.

Nomenclature

$\boldsymbol{A}$, $\boldsymbol{D}$	=	laminate in-plane and transverse stiffness matrices
$\boldsymbol{A}^*$, $\boldsymbol{D}^*$	=	matrices of in-plane and flexural flexibility in partially inverted laminate constitutive equations
$\boldsymbol{B}$	=	laminate coupling stiffness matrix
$\boldsymbol{B}^*$	=	coupling matrix in partially inverted laminate constitutive equations
e	=	eccentricity
$\boldsymbol{e}$	=	vector of eccentricity coefficients e_j
e_i	=	generalized coordinates of the neutral plane function
$\boldsymbol{G}$, $\boldsymbol{H}$, $\bar{\boldsymbol{H}}$	=	matrices defined in Eqs. (44–46)
l_x, l_y	=	length and width of panel
$\boldsymbol{N}$, $\boldsymbol{M}$	=	unit width stresses and bending moment vectors
N_x, N_y, N_{xy}	=	internal in-plane loads per unit width
$N_{x,o}$, $N_{y,o}$, $N_{xy,o}$	=	external in-plane loads per unit width
$\boldsymbol{Q}$	=	vector defined in Eq. (19)
$\boldsymbol{u_0}$, $\boldsymbol{v_0}$	=	in-plane displacement of neutral plane in x and y directions
w	=	out-of-plane displacement
w_i	=	generalized coordinates of the displacement function
X, Y, $\bar{X}$, $\bar{Y}$	=	beam eigenfunctions
Γ_x, Γ_y, Γ_{xy}	=	circulation functions
$\Delta\Psi$	=	equilibrium stress function for perturbation loading
ε_x, ε_y, ε_{xy}	=	in-plane strains
ε_x^0, ε_y^0, ε_{xy}^0	=	in-plane strains at neutral plane level
η_j	=	eigenfunctions of compatibility stress function
ξ_j	=	generalized coordinates of the compatibility stress function
Π	=	total potential
Π_N	=	total potential of internal in-plane loads
Π_Q	=	potential of external transverse loads
Π_w	=	internal elastic potential energy
φ_j	=	transverse displacement eigenfunctions
$\bar{\varphi}_j$	=	eccentricity eigenfunctions
ϕ_n	=	weight functions
Ψ	=	equilibrium stress function for uniform loading
Ψ_c	=	compatibility stress function
Ψ_e	=	equilibrium stress function
Ω	=	stress function

Presented as Paper 2455 at the 50th AIAA/ASME/ASCE/AHS/ASC Structures, Structural Dynamics, and Materials Conference, Palm Springs, CA, 4–7 May 2009; received 31 March 2009; revision received 11 May 2009; accepted for publication 11 May 2009.

*Golf Course Lane; enzo.cosentino@airbus.com (Corresponding Author).
†Queen's Building, University Walk.

I. Introduction

WITH the introduction of the total carbon design philosophy in aircraft structures, it is becoming increasingly important to obtain further weight savings with composite cocured/cobonded assemblies. Sizing of composite stringer terminations is becoming one of the most critical phases of preliminary design of novel aircraft because of the potential for significant weight savings. In stiffened aircraft panels, it is often necessary to terminate the stringer at a particular location within the span because of the taper angle in the wings (Fig. 1), or because of other features, such as cutouts, manholes, or passenger/cargo doors in the fuselage.

In cocured and cobonded skin/stringer panels with stringer terminations, failure often occurs due to delamination and/or debonding between skin and stiffener at the stiffener's foot tip. Such failure is in contrast to overall strain limitations and usually occurs at much lower levels. Several past and recent studies [1–4], have shown that the onset of debonding may be caused by differential stiffness at the interface between the skin and the cocured/cobonded surface. Skin deflection due to eccentricity of the in-plane loads and/or pressure causes the onset of peeling moments and membrane tractions that trigger the first and the second crack opening modes [5].

Furthermore, stress concentrations and free edge effects, due to anisotropy, can exacerbate the failure phenomenon by triggering significant localized through-thickness effects. Currently, the most accepted designs entail running the stiffener out midbay (Fig. 1b), or at rib locations to minimize the peeling phenomena (Fig. 1a). Yet, the latter design solution requires the skin to be thickened by adding

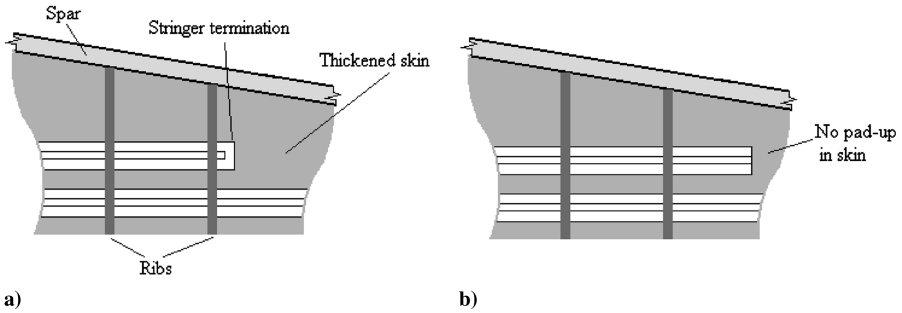

Fig. 1 Stringer terminated: a) under the rib and b) midbay.

local pad-up [6] to avoid premature skin buckling onset; thus adding undesirable and penalizing extra weight. In fact, it is a currently accepted design requirement that this type of structure cannot buckle below design limit loads [7]. The constraint can be even more restrictive for thick-sectioned panels that are sometimes not allowed to buckle before the design ultimate load. These limiting constraints are mostly due to the lack of methodical understanding of the causes of disbond and the structural behavior after a crack/disbond initiates. Falzon and Davies [6] have shown that in the prebuckling regime, failure often occurs due to crack initiation at critical locations (Fig. 2).

Falzon and Davies [4] proposed a finite element model (FEM) to predict crack initiation in unbuckled panels, which shows good correlation with tests. Meeks et al. [7] demonstrated that the same failure mechanism occurs in postbuckled structures, confirming that the disbond is the main failure mode for composite assemblies undergoing large transverse displacements. Despite the fact that FEM has proven able to provide realistic predictions of initial disbond [8], the large computational times, in conjunction with the rather significant sensitivity of the results to the mesh size, hinder its use as a main tool for preliminary phases of aircraft design. There is an objective need for simple analytical solutions that guarantee considerable reduction of computational efforts, yet capture the essential mechanics of the problem. Furthermore, a major advantage related to closed-form solutions is that they are readily implementable in parametric form for optimization techniques.

Mittelstedt [9] proposed a closed-form solution for buckling of composite assemblies with periodic boundary conditions. Results were encouraging but unfortunately not applicable to panels with stringer terminations. In such structures, the eccentricity of the in-plane loads induces localized transverse bending, which affects the prebuckling behavior, and could significantly influence calculation of buckling loads. Cosentino and Weaver [10] proposed an analytical linear approach for accurate calculation of buckling loads of panels with stringer terminations. The novelty of the approach was in the modeling of the in-plane loads redistribution induced by the perturbation of a discontinuous stiffener within the panel. The model works well when applied to structures with negligible flexural and membrane anisotropy, but its predictions might be inaccurate when these effects become significant. In some cases, and especially in thin-walled configurations, panels that are unsymmetrically laminated or symmetric but not balanced, can exhibit a material induced coupling between membrane and flexural response or axial and shear in-plane deformations, respectively. For example, let us isolate a panel from the surrounding structure. If the panel is loaded in axial compression, in which the two opposite unloaded edges are totally or partially restrained against Poisson's ratio effects and shearing deformations, then additional kinematically induced shearing and transverse axial loads are induced, which can be significantly large [11]. As a result, the prebuckling deformed shapes, the buckling loads, and the buckling modes could be appreciably affected because the deformed configurations are skewed in appearance.

This work aims to develop a fast and reliable approach for the calculation of buckling loads of composite panels with stringer terminations to be used in conjunction with a method to predict disbond in the prebuckling regime. This analysis improves the method for disbond prediction proposed by Cosentino and Weaver [5] in terms of mechanical response and provides an accurate analytical calculation of the critical buckling loads. Indeed, if the analyzed structure is not allowed to buckle, it is essential to ensure that the calculated disbond loads do not exceed the critical buckling loads. Therefore, a self-contained approach that is reliable, robust, and which does not require extreme computational efforts is presented.

II. Outline of the Approach

The purpose of this analysis is to establish a methodology to accurately predict buckling loads of unsymmetrically laminated composite panels with stringer terminations. To achieve this, expressions are developed which govern the prebuckling regime in terms of deformations and stress redistributions.

Two coupled nonlinear equations (namely, transverse equilibrium and compatibility) are derived in Sec. III that use the transverse displacement and Airy's stress function. To facilitate an analytical solution to the inherently nonlinear, coupled fourth-order differential equations, a simplifying step-by-step- procedure is developed. First, the discontinuous stiffnesses $\boldsymbol{A}^*$ and $\boldsymbol{B}^*$ are represented in continuous form by a generalized Fourier series to allow a Galerkin representation of the compatibility equation. The eccentricity e is represented in continuous form by a generalized Fourier series to allow a Rayleigh–Ritz representation of transverse equilibrium. Then the Airy's stress function Ω is modeled as the sum of two functional components:

1) An equilibrium stress function Ψ_e comprises two components: one fulfills the in-plane equilibrium and the mechanical boundary conditions Ψ_0, and the other satisfies the perturbation to the stress field due to the stiffener, Δ_Ψ. This function alone only satisfies the equilibrium and compatibility equations governing the isotropic case.

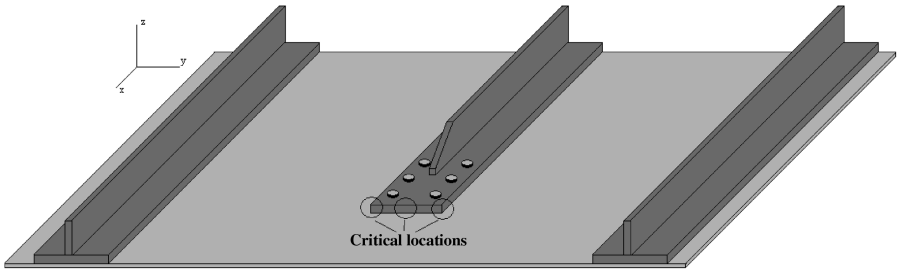

Fig. 2 Critical locations in composite panel with stringer termination.

2) A compatibility stress function Ψ_c is introduced to satisfy the compatibility equation in terms of orthotropy and anisotropy. Ψ_c takes into account the perturbation induced by asymmetry and orthotropy and is expanded in a generalized Fourier series. To not perturb the global internal and boundary equilibrium already satisfied by the equilibrium stress function Ψ_e, a particular form was chosen for Ψ_c. The function satisfies the nullity of mechanical boundary conditions in conjunction with average nullity of the internal loads.

To find particular solutions in closed form, the boundary conditions must be determined a priori. This is done by schematizing the domain as a system of springs in series and parallel [10].

A hybrid Ritz/Galerkin solution strategy was used to solve the two nonlinear equations. The transverse equilibrium equation was solved using an energy based Rayleigh–Ritz technique in conjunction with the Castigliano's principle of least work. A Galerkin technique was employed to discretize and solve the compatibility equation. The strategy chosen allows the derivation of analytical Fourier series expansions for both the transverse displacement and the Airy's stress function, which intrinsically satisfy the natural boundary conditions. As such, no additional calculations are required to minimize induced errors, thus improving the performances of the proposed methodology in terms of calculation time.

In the following sections it will be shown that satisfying equilibrium and compatibility equations is a key requisite to capture the significant in-plane stress redistributions that affect the structural behavior of eccentric structures. The calculation of buckling loads is performed by means of an ad-hoc iterative algorithm. Rationales for the algorithm and convergence studies are provided in Secs. IV and V.

III. Prebuckling Model Derivation

Let us focus on a composite panel with a stringer terminated within the bay (Fig. 3). To employ the classical two-dimensional theory of plates, the three-dimensional assembly depicted in Fig. 3a is reduced to the equivalent single layer represented in Fig. 3b. The use of von Kármán's nonlinear field equations allows two variables only: that is, the transverse deflection w and the stress function Ω, to be fully representative of the state of stress throughout the domain [10]. Following Cosentino and Weaver [8], the beam properties of the stiffeners are locally homogenized over the plate as represented in Fig. 4b. The global domain is therefore partitioned into subdomains (fields). Different sets of $\boldsymbol{A}$, $\boldsymbol{B}$, and $\boldsymbol{D}$ matrices and local value of eccentricity e are assigned to each subdomain (Fig. 4).

Three different subdomains are identified: 1) skin subdomain, 2) skin/flange subdomain, and 3) skin/flange/web subdomain.

Each variable is hereby indicated with the subscript s, sf, and sfw, when referring to the value of that variable over the skin, skin/flange, and skin/flange/web subdomains, respectively.

Following von Kármán , the membrane strains and the curvatures are expressed as functions of the transverse displacement as follows:

$$\varepsilon_x^0 = \frac{\partial u_o}{\partial x} + \frac{1}{2}\left(\frac{\partial w}{\partial x}\right)^2, \qquad \varepsilon_{xy}^0 = \frac{\partial u_0}{\partial y} + \frac{\partial v_0}{\partial x} + \frac{\partial w}{\partial x}\frac{\partial w}{\partial y}$$
$$\varepsilon_y^0 = \frac{\partial v_0}{\partial y} + \frac{1}{2}\left(\frac{\partial w}{\partial y}\right)^2 \tag{1}$$

$$k_x = -\frac{\partial^2 w}{\partial x^2}, \qquad k_x = -\frac{\partial^2 w}{\partial y^2}, \qquad k_{xy} = -2\frac{\partial^2 w}{\partial x \partial y} \tag{2}$$

It is assumed that all of the considered assemblies are sufficiently thin, so that both of the preceding kinematical assumptions and the plane state of stress required by classical laminate theory are satisfied. According to this assumption, the constitutive equations of the laminate expressed in the partially inverted form are [12]

$$\begin{bmatrix} \boldsymbol{\varepsilon}^0 \\ \boldsymbol{M} \end{bmatrix} = \begin{bmatrix} \boldsymbol{A}^* & \boldsymbol{B}^* \\ -\boldsymbol{B}^{*T} & \boldsymbol{D}^* \end{bmatrix} \begin{bmatrix} \boldsymbol{N} \\ \boldsymbol{k} \end{bmatrix} \tag{3}$$

A stress function Ω is introduced such that

$$N_x = \Omega_{,yy}, \qquad N_y = \Omega_{,xx}, \qquad N_{xy} = -\Omega_{,xy} \tag{4}$$

The first governing equation of the elastic problem is the transverse equilibrium equation, which is derived according to the principle of stationary potential energy [8]:

$$\partial(\Pi_w + \Pi_N + \Pi_Q) = 0 \tag{5}$$

where

$$\Pi_w = \frac{1}{2}\int_0^{l_x}\int_0^{l_y} \boldsymbol{k}^T \boldsymbol{M}\, \mathrm{d}x\, \mathrm{d}y = \frac{1}{2}\int_0^{l_x}\int_0^{l_y} \boldsymbol{k}^T \boldsymbol{D}^* \boldsymbol{k}\, \mathrm{d}x\, \mathrm{d}y$$
$$= \frac{1}{2}\int_0^{l_x}\int_0^{l_y}\left[D_{11}^*\left(\frac{\partial^2 w}{\partial x^2}\right)^2 + D_{22}^*\left(\frac{\partial^2 w}{\partial y^2}\right)^2 + 4D_{66}^*\left(\frac{\partial^2 w}{\partial x \partial y}\right)^2 + 2D_{12}^*\frac{\partial^2 w}{\partial x^2}\frac{\partial^2 w}{\partial y^2} + 4D_{16}^*\frac{\partial^2 w}{\partial x^2}\frac{\partial^2 w}{\partial x \partial y} + 4D_{26}^*\frac{\partial^2 w}{\partial y^2}\frac{\partial^2 w}{\partial x \partial y}\right]\mathrm{d}x\, \mathrm{d}y \tag{6}$$

$$\Pi_N = \frac{1}{2}\int_0^{l_x}\int_0^{l_y}\left[\Omega_{,yy}\left(\frac{\partial w}{\partial x} + \frac{\partial e}{\partial x}\right)^2 + \Omega_{,xx}\left(\frac{\partial w}{\partial y} + \frac{\partial e}{\partial y}\right)^2 + 2\Omega_{,xy}\frac{\partial (w+e)}{\partial x}\frac{\partial (w+e)}{\partial y}\right]\mathrm{d}x\, \mathrm{d}y \tag{7}$$

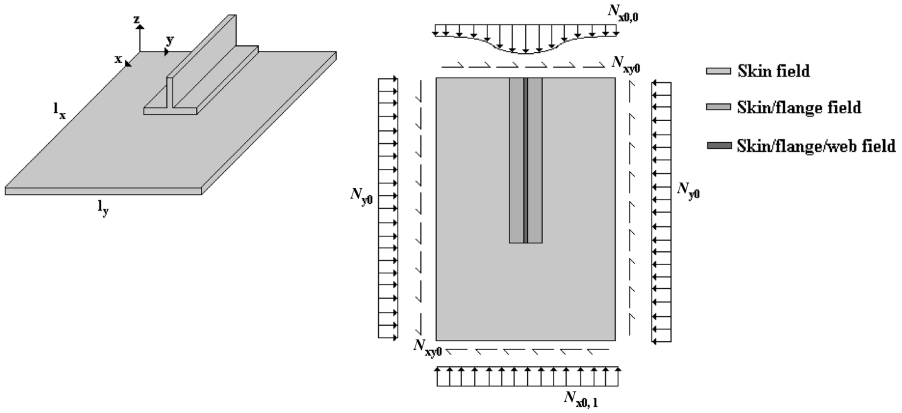

Fig. 3 Analyzed structure: a) three-dimensional representation, and b) equivalent two-dimensional single layer scheme.

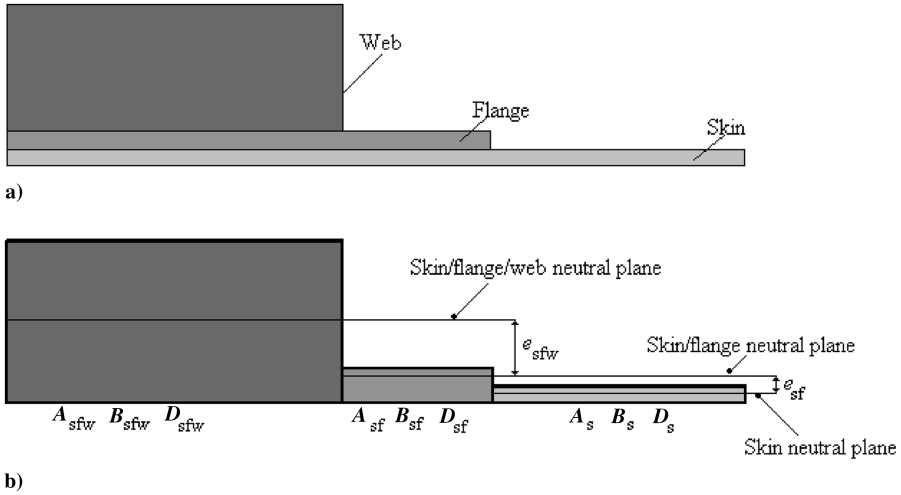

Fig. 4 Longitudinal section: a) real structure and b) properties condensation.

$$\Pi_Q = -\int_0^{l_x}\int_0^{l_y} qw\,\mathrm{d}x\,\mathrm{d}y \tag{8}$$

The second governing equation is the compatibility equation, which under the assumption of linear elasticity reads [13]

$$\begin{aligned}&\frac{\partial^2}{\partial y^2}(A_{11}^*\Omega_{,yy} + A_{12}^*\Omega_{,xx} - A_{16}^*\Omega_{,xy} - B_{11}^* w_{,xx} - B_{12}^* w_{,yy}\\ &\quad - 2B_{16}^* w_{,xy}) + \frac{\partial^2}{\partial x^2}(A_{12}^*\Omega_{,yy} + A_{22}^*\Omega_{,xx} - A_{26}^*\Omega_{,xy} - B_{21}^* w_{,xx}\\ &\quad - B_{22}^* w_{,yy} - 2B_{26}^* w_{,xy}) + \frac{\partial^2}{\partial x\partial y}(-A_{16}^*\Omega_{,yy} - A_{26}^*\Omega_{,xx}\\ &\quad + A_{66}^*\Omega_{,xy} + B_{61}^* w_{,xx} + B_{62}^* w_{,yy} + 2B_{66}^* w_{,xy}) = 0\end{aligned} \tag{9}$$

Differentiation and reordering gives

$$\begin{aligned}&A_{11}^*\Omega_{,yyyy} - 2A_{26}^*\Omega_{,xyyy} + (2A_{12}^* + A_{66}^*)\Omega_{,xxyy} - 2A_{26}^*\Omega_{,xxxy}\\ &\quad + A_{22}^*\Omega_{,xxxx} + (2A_{11,y}^* - A_{16,x}^*)\Omega_{,yyy} + (2A_{12,x}^* - 3A_{16,y}^*\\ &\quad + A_{66,x}^*)\Omega_{,xyy} + (2A_{12,y}^* - 3A_{26,x}^* + A_{66,y}^*)\Omega_{,xxy} + (2A_{22,x}^*\\ &\quad - A_{26,y}^*)\Omega_{,xxx} + (A_{11,yy}^* + A_{12,xx}^* - A_{16,xy}^*)\Omega_{,yy} - (A_{16,yy}^*\\ &\quad + A_{26,xx}^* - A_{66,xy}^*)\Omega_{,xy} + (A_{12,yy}^* + A_{22,xx}^* - A_{26,xy}^*)\Omega_{,xx}\\ &\quad - B_{21}^* w_{,xxxx} + (B_{61}^* - 2B_{26}^*)w_{,xxxy} + (2B_{66}^* - B_{11}^*\\ &\quad - B_{22}^*)w_{,xxyy} + (B_{62}^* - 2B_{16}^*)w_{,xyyy} - B_{12}^* w_{,yyyy} - (B_{61,y}^*\\ &\quad - 2B_{21,x}^*)w_{,xxx} + (2B_{66,y}^* + B_{61,x}^* - 2B_{11,y}^* - 4B_{26,x}^*)w_{,xxy}\\ &\quad + (2B_{66,x}^* + B_{62,y}^* - 2B_{22,x}^* - 4B_{16,y}^*)w_{,xyy} + (B_{62,x}^*\\ &\quad - 2B_{12,y}^*)w_{,yyy} + (B_{61,xy}^* - B_{11,yy}^* - B_{21,xx}^*)w_{,xx} + 2(B_{66,xy}^*\\ &\quad - B_{16,yy}^* - B_{26,xx}^*)w_{,xy} + (B_{62,xy}^* - B_{12,yy}^* - B_{22,xx}^*)w_{,xx} = 0\end{aligned} \tag{10}$$

To solve Eqs. (5) and (10) by means of Rayleigh–Ritz and/or the Galerkin technique, suitable generalized Fourier series expansions for the two variables of interest, w and Ω, are sought. The same kind of expansions are required for the eccentricity e and the components of $\boldsymbol{A}^*$ and $\boldsymbol{B}^*$ matrices. These parameters are already defined in a discontinuous piecewise form over the entire domain (Figs. 3b and 4b). Nevertheless, Eqs. (5) and (10) require these parameters to be expressed in a continuous and differentiable form.

The following expressions are suitable for the transverse displacement w, the eccentricity e, and the components of the matrices $\boldsymbol{A}^*$ and $\boldsymbol{B}^*$ [8], [10]:

$$w = \sum_{i=1}^{M\times N} w_i\varphi_i(x,y) \tag{11a}$$

$$e = \sum_{k=1}^{\bar{M}\times\bar{N}} e_k\bar{\varphi}_k(x,y) \tag{11b}$$

$$A_{ij}^* = A_{ij,s}^* + \sum_{k=1}^{\bar{M}\times\bar{N}} a_{ij,k}^*\bar{\varphi}_k \tag{12a}$$

$$B_{ij}^* = B_{ij,s}^* + \sum_{k=1}^{\bar{M}\times\bar{N}} b_{ij,k}^*\bar{\varphi}_k \tag{12b}$$

where

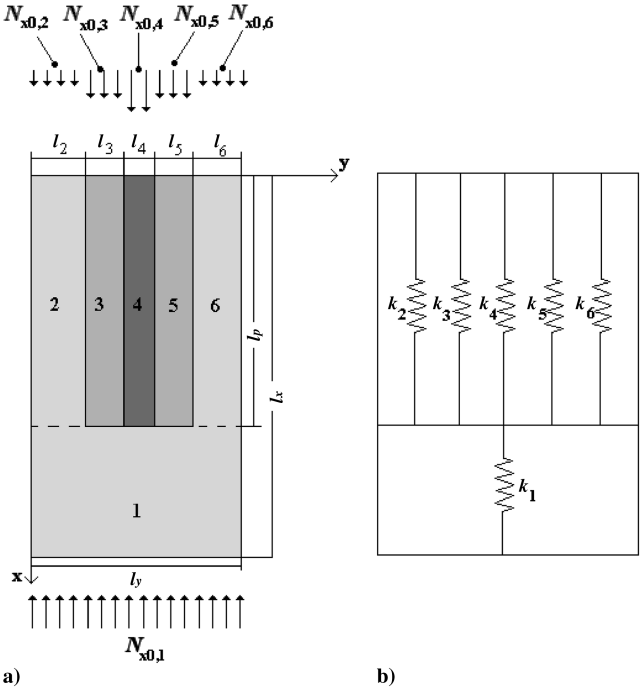

Fig. 5 Domain schematization for edge axial *x*wise loads derivation.

$$\varphi = [\,X_1Y_1 \quad X_1Y_2, \ldots, X_1Y_{N_w} \quad X_2Y_1 \quad X_2Y_2, \ldots, X_2Y_N, \ldots, X_MY_1 \quad X_MY_2 \quad X_MY_N\,]^T, \qquad \boldsymbol{W} = [\,w_1 \quad w_2, \ldots, w_{M\times N}\,]^T \tag{13}$$

$$\bar{\varphi} = [\,\bar{X}_1\bar{Y}_1 \quad \bar{X}_1\bar{Y}_2, \ldots, \bar{X}_1\bar{Y}_{\bar{N}} \quad \bar{X}_2\bar{Y}_1 \quad \bar{X}_2\bar{Y}_2, \ldots, \bar{X}_2\bar{Y}_{\bar{N}}, \ldots, \bar{X}_{\bar{M}}\bar{Y}_1 \quad \bar{X}_{\bar{M}}\bar{Y}_2 \quad \bar{X}_{\bar{M}}\bar{Y}_{\bar{N}}\,]^T, \qquad \mathbf{e} = [\,e_1 \quad e_2, \ldots, e_{\bar{M}\times\bar{N}}\,]^T \tag{14}$$

Functions $X_m(x)$, $Y_n(y)$, $\bar{X}_m(x)$, and $\bar{Y}_n(y)$ are continuous and indefinitely differentiable. Where possible, it is recommended to use beam eigenfunctions that satisfy Hilbert's orthogonality relations [8] and essential (kinematical) boundary conditions for both the transverse displacement and the neutral plane function.

The coefficients e_k, $a^*_{ij,k}$, and $b^*_{ij,k}$ are calculated by means of a Galerkin technique and expressed as follows:

$$e_k = \boldsymbol{K}^{-1}_{kq}\boldsymbol{E}_q \tag{15a}$$

$$a^*_{ij,k} = \boldsymbol{K}^{-1}_{kq}\boldsymbol{\alpha}_{ij,q} \tag{15b}$$

$$b^*_{ij,k} = \boldsymbol{K}^{-1}_{kq}\boldsymbol{\beta}_{ij,q} \tag{15c}$$

where

$$\boldsymbol{E}_q = \int_{x=0}^{l_x}\int_{y=0}^{l_y} e(x,y)\bar{\varphi}_q(x,y)\,\mathrm{d}x\,\mathrm{d}y \tag{16}$$

$$\boldsymbol{\alpha}_{ij,q} = \int_{x=0}^{l_x}\int_{y=0}^{l_y} (A^*_{ij} - A^*_{ij,s})\bar{\varphi}_q(x,y)\,\mathrm{d}x\,\mathrm{d}y \tag{17a}$$

$$\beta_{ij,q} = \int_{x=0}^{l_x}\int_{y=0}^{l_y} (B^*_{ij} - B^*_{ij,s})\bar{\varphi}_q(x,y)\,\mathrm{d}x\,\mathrm{d}y \tag{17b}$$

$$K_{kq} = \int_{x=0}^{l_x}\int_{y=0}^{l_y} \bar{\varphi}_k(x,y)\bar{\varphi}_q(x,y)\,\mathrm{d}x\,\mathrm{d}y \tag{18}$$

The expansion of the stress function Ω in a generalized Fourier series is not straightforward and requires a number of steps. Essentially, it is decomposed into two components: Ψ_e and Ψ_c. The approach used by Cosentino and Weaver [10] is followed in the present analysis and briefly described in the following. To evaluate Ψ_e, let us consider the panel sketched in Fig. 3b. The first step is to quantitatively capture the natural boundary conditions. To do this, an approximate technique is used. Let us assume that the panel is clamped on the edge $x = 0$ and loaded by a uniform axial load per unit width $N_{x0,L}$ on the edge $x = l_x$. The presence of the stiffener induces in-plane load redistribution. It is reasonable to expect the load to be channeled through the skin/flange and the skin/flange/web area, which, as such, carry more load than the skin. The in-plane state of stress is described by a stress function, and in order to choose a suitable expression for this, the natural (mechanical) boundary conditions must be determined a priori.

To derive an approximate axial flow piecewise distribution along the clamped edge $x = 0$ (Fig. 5a), the following assumptions are taken:

1) The in-plane unit width loads N_{xi} are assumed to be constant within each subdomain, which may be represented as a spring with a concentrated stiffness.

2) Every straight line parallel to the y axis remains straight after deformation.

These assumptions do not represent the real state of stress throughout the domain. However, they are only used to calculate the natural boundary conditions to be assigned to the stress function. Nonetheless, because only the stress field at the boundary is of interest at this stage, the assumption of discrete variation of N_x is not restrictive if the stringer length is sufficiently large (i.e., l_x/l_p is sufficiently large and l_x/l_p is also not too small). In such cases, the skin-to-stiffener load transfer is already completed far from the boundary, and we may assume that the uniform axial ($x$wise) strain condition is reestablished on the two opposite edges $x = 0$ and l_x at a minimum. This description is an adequate representation of actual stiffener run-outs in stiffened panels.

Under these assumptions, the whole domain is schematized as a system of springs in series and in parallel (Fig. 5b). After algebraic manipulations, the following expressions for the piecewise edge load distribution are obtained:

$$N_{x0,i} = \frac{A_{11,i}l_y}{\sum_{i=2}^{6}\frac{l_{x,i}}{A'_{11,i}}}N_{x0,l} \quad \forall\ i = 2, \ldots, 6 \tag{19}$$

Once the natural boundary conditions are determined for the edge $x = 0$ (in piecewise form) and for the edge $x = l_x$, both distributions can be expanded in a Fourier series:

$$N_{xo}|_{x=0} \cong \sum_{n=1}^{N^*} A_n \sin(\alpha_n y) \tag{20a}$$

$$N_{xo}|_{x=l_x} \cong \sum_{n=1}^{N^*} B_n \sin(\alpha_n y) \tag{20b}$$

Let us focus on the generic nth components of the series (20a) and (20b) acting on the edges $x = 0$ and l_x, respectively (Fig. 6a).

Using the principle of superposition, the generic stress field represented in Fig. 6a can be decomposed into two stress fields. Because the coefficients B_n represents the Fourier's expansion of the constant in-plane stress applied on the edge $x = l_x$, the two stress fields schematized in Fig. 6b and 6c are 1) a constant axial stress field equal to the constant axial load $N_{x0,l}$ acting upon the free edge $x = l_x$ (Fig. 6b) and 2) a perturbation $\Delta N_x = N_{x0,l} - N_{x0,0}$ caused by the presence of the reinforcement (Fig. 6c) and acting as an external load on the constrained edge.

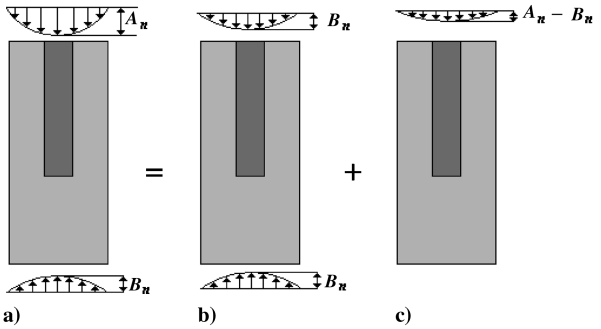

Fig. 6 Reinforced panel: a) loaded by generalized Fourier series components of loads, b) uniform loading for the equal expansion coefficients, and c) reinforcement perturbation. The first components are shown for illustrative purposes only.

The first stress field is constant and represents a uniform axial ($x$wise) loading condition; therefore, it is equilibrated and compatible. The elastic problem is completely determined by introducing the stress function Ψ:

$$\Psi_0 = \Gamma_x N_{x0,l} + \Gamma_{xy} N_{xy0} + \Gamma_y N_{y0} \tag{21}$$

where Γ_x, Γ_{xy}, and Γ_y are the circulation functions [14] defined as

$$\Gamma_x = (y - l_y)^2 \tag{22a}$$

$$\Gamma_{xy} = -(x - l_x)(y - l_y) \tag{22b}$$

$$\Gamma_y = (x - l_x)^2 \tag{22c}$$

The second stress field represents the boundary perturbation introduced by the presence of the reinforcement. It is observed that following this approach permits Fourier series expansion in only the perturbation of the total load from the constant axial distribution $N_{xo,l}$ (Fig. 5). This perturbation occurs at the edge $x = 0$ and is such that the total force resultant over the width is equal to zero.

The solution in terms of stress function was found by Timoshenko and Goodier [15]:

$$\Delta\Psi = \sum_{n=1}^{N^*} \Delta\Psi_n = \sum_{n=1}^{N^*} \sin(\alpha_n y) f_n(x) \tag{23}$$

where the $x$wise function $f_n(x)$ is in the form

$$f_n(x) = c_{1n}\cosh(\alpha_n x) + c_{2n}\sinh(\alpha_n x) + c_{3n} x\cosh(\alpha_n x) + c_{4n} x\sinh(\alpha_n x) \tag{24}$$

Applying appropriate boundary conditions, the coefficients of integration are obtained as

$$c_{1n} = \lambda_{1n}(A_n - B_n) \tag{25a}$$

$$c_{2n} = \lambda_{2n}(A_n - B_n) \tag{25b}$$

$$c_{3n} = \lambda_{3n}(A_n - B_n) \tag{25c}$$

$$c_{4n} = \lambda_{4n}(A_n - B_n) \tag{25d}$$

where

$$\lambda_{1n} = \frac{1}{\alpha_n^2} \tag{26a}$$

$$\lambda_{2n} = \frac{1 - \omega_{1n}\sinh(\alpha_n l_x)}{l_x \alpha_n^3} \tag{26b}$$

$$\lambda_{3n} = \frac{1 - (\omega_{1n}/\omega_{21n})\sinh(\alpha_n l_x)}{l_x \alpha_n^2} \tag{26c}$$

$$\lambda_{4n} = -\frac{\sinh(\alpha_n l_x)}{l_x \alpha_n \omega_{2n}} \tag{26d}$$

and

$$\omega_{1n} = \frac{\cot(\alpha_n)}{\alpha_n} + \frac{1}{l_x \alpha_n^2} \tag{27a}$$

$$\omega_{2n} = (\sin(\alpha_n) - l_x \alpha_n \cos(\alpha_n))\omega_{1n} + l_x \sin(\alpha_n) \tag{27b}$$

Using the principle of superposition, the resultant stress function Ψ_e is

$$\Psi_e = \Psi_0 + \sum_{n=1}^{N^*} \Delta\Psi_n \tag{28}$$

This function satisfies the following biharmonic equation:

$$\frac{\partial^4 \Psi_e}{\partial y^4} + 2\frac{\partial^4 \Psi_e}{\partial x^2 \partial y^2} + \frac{\partial^4 \Psi_e}{\partial x^4} = 0 \tag{29}$$

Equation (29) is the expression of the compatibility equation for isotropic plates [15], in which the in-plane equilibrium is satisfied because of the properties (4) of the stress function used. Ψ_e represents a particular solution of the isotropic elastic problem. As such, it does not satisfy the compatibility Eq. (10). To enforce the compatibility condition, a supplementary stress function Ψ_c is superposed, which takes in to account the effect of orthotropy and anisotropy. The additional stress function that must guarantee the resultant stress function Ω,

$$\Omega = \Psi_e + \Psi_c \tag{30}$$

satisfies the compatibility Eq. (10).

The equilibrium and boundary conditions are fulfilled by choosing the supplementary stress function as

$$\Psi_c = \sum_{n=1}^{N_c} \Psi_{c_n} = \sum_{n=1}^{N_c} \xi_n \eta_n(x, y) = \sum_{n=1}^{N_c} \xi_n \cos(\alpha_n y) g_n(x) \tag{31}$$

where ξ_n are unknown coefficients and the $x$wise functions $f_n(x)$ are in the form

$$g_n(x) = g_{1n}\cosh(\alpha_n x) + g_{2n}\sinh(\alpha_n x) + g_{3n} x\cosh(\alpha_n x) + g_{4n} x\sinh(\alpha_n x) + g_{5n} \tag{32}$$

The use of cosine functions as basis functions for the Fourier expansion guarantees satisfaction of $x$wise equilibrium in terms of total axial load:

$$\int_0^{l_y} N_x \, dy = \int_0^{l_y} \frac{\partial^2}{\partial y^2} \Delta\Psi \, dy = -\alpha_n^2 \int_0^{l_y} \sin(\alpha_n y) f_n(x) \, dy = 0 \quad \forall\ x \tag{33}$$

Coefficients g_{1n}, g_{2n}, g_{3n}, and g_{4n} can be calculated from Eqs. (25–27) by ensuring that the null loading condition is satisfied by $A_n = 1$ and $B_n = -1$ and then substituting g_{1n}, g_{2n}, g_{3n}, and g_{4n} for c_{1n}, c_{2n}, c_{3n}, and c_{4n}, respectively. The coefficient g_{5n} was introduced to enforce nullity at edges $x = 0$ and l_x.

Equation (33) represents the condition that the total axial load introduced by the compatibility stress function is averagely null along every $x$wise cross section of the panel. Therefore, because of the linearity of the biharmonic equilibrium equation, the resultant stress function $\Omega = \Psi_e + \Psi_c$ satisfies the following biharmonic isotropic equation in the average sense:

$$\int_0^{l_y} \left(\frac{\partial^4 \Omega}{\partial y^4} + 2\frac{\partial^4 \Omega}{\partial x^2 \partial y^2} + \frac{\partial^4 \Omega}{\partial x^4} \right) dy = 0 \quad \forall\ x \tag{34}$$

The fulfillment of the compatibility Eq. (10) is obtained by using a Galerkin technique, as shown in Sec. IV.

IV. Prebuckling Model: Quasi-Nonlinear Solution Strategy

The two governing equations (5) and (10) represent a system of nonlinear coupled equations in w and Ω. The nonlinearity is due to

the transverse equilibrium Eq. (5), in which coupled products of the in-plane stress function and transverse displacements are present. Nevertheless, a more accurate analysis of the compatibility Eq. (10) might be useful to approximate the solution. Substituting expressions (11a) and (30) in Eq. (10) and carrying out the differentiations after algebraic manipulations, we obtain

$$\sum_{k=1}^{M_c\times N_c} L_{\xi,k}\xi_k + \sum_{j=1}^{M\times N} L_{w,j}w_j = L_\Delta + L_x N_{x0,l} + L_{xy}N_{xy0} + L_y N_{y0} \tag{35}$$

where

$$\begin{aligned} L_{\xi_k} &= A^*_{11}\eta_{k,yyyy} - 2A^*_{26}\eta_{k,xyyy} + (2A^*_{12} + A^*_{66})\eta_{k,xxyy} \\ &\quad - 2A^*_{26}\eta_{k,xxxy} + A^*_{22}\eta_{k,xxxx} + (2A^*_{11,y} - A^*_{16,x})\eta_{k,yyy} \\ &\quad + (2A^*_{12,x} - 3A^*_{16,y} + A^*_{66,x})\eta_{k,xyy} + (2A^*_{12,y} - 3A^*_{26,x} \\ &\quad + A^*_{66,y})\eta_{k,xxy} + (2A^*_{22,x} - A^*_{26,y})\eta_{k,xxx} + (A^*_{11,yy} + A^*_{12,xx} \\ &\quad - A^*_{16,xy})\eta_{k,yy} - (A^*_{16,yy} + A^*_{26,xx} - A^*_{66,xy})\eta_{k,xy} \\ &\quad + (A^*_{12,yy} + A^*_{22,xx} - A^*_{26,xy})\eta_{k,xx} \end{aligned} \tag{36}$$

$$\begin{aligned} L_{w_j} &= -B^*_{21}\varphi_{j,xxxx} + (B^*_{61} - 2B^*_{26})\varphi_{j,xxxy} + (2B^*_{66} - B^*_{11} \\ &\quad - B^*_{22})\varphi_{j,xxyy} + (B^*_{62} - 2B^*_{16})\varphi_{j,xyyy} - B^*_{12}\varphi_{j,yyyy} - (B^*_{61,y} \\ &\quad - 2B^*_{21,x})\varphi_{j,xxx} + (2B^*_{66,y} + B^*_{61,x} - 2B^*_{11,y} - 4B^*_{26,x})\varphi_{j,xxy} \\ &\quad + (2B^*_{66,x} + B^*_{62,y} - 2B^*_{22,x} - 4B^*_{16,y})\varphi_{j,xyy} + (B^*_{62,x} \\ &\quad - 2B^*_{12,y})\varphi_{j,yyy} + (B^*_{61,xy} - B^*_{11,yy} - B^*_{21,xx})\varphi_{j,xx} + 2(B^*_{66,xy} \\ &\quad - B^*_{16,yy} - B^*_{26,xx})\varphi_{j,xy} + (B^*_{62,xy} - B^*_{12,yy} - B^*_{22,xx})\varphi_{j,xx} = 0 \end{aligned} \tag{37}$$

$$\begin{aligned} L_\Delta &= -[A^*_{11}\Delta\Psi_{,yyyy} - 2A^*_{26}\Delta\Psi_{,xyyy} + (2A^*_{12} + A^*_{66})\Delta\Psi_{,xxyy} \\ &\quad - \Delta\Psi_{,xxxy}A^*_{26} + A^*_{22}\Delta\Psi_{,xxxx} + (2A^*_{11,y} - A^*_{16,x})\Delta\Psi_{,yyy} \\ &\quad + (2A^*_{12,x} - 3A^*_{16,y} + A^*_{66,x})\Delta\Psi_{,xyy} + (2A^*_{12,y} - 3A^*_{26,x} \\ &\quad + A^*_{66,y})\Delta\Psi_{,xxy} + (2A^*_{22,x} - A^*_{26,y})\Delta\Psi_{,xxx} + (A^*_{11,yy} + A^*_{12,xx} \\ &\quad - A^*_{16,xy})\Delta\Psi_{,yy} - (A^*_{16,yy} + A^*_{26,xx} - A^*_{66,xy})\Delta\Psi_{,xy} \\ &\quad + (A^*_{12,yy} + A^*_{22,xx} - A^*_{26,xy})\Delta\Psi_{,xx}] \end{aligned} \tag{38}$$

$$L_x = -(A^*_{11,yy} + A^*_{12,xx} - A^*_{16,xy}) \tag{39a}$$

$$L_{xy} = -(A^*_{16,yy} + A^*_{26,xx} - A^*_{66,xy}) \tag{39b}$$

$$L_{xy} = (A^*_{12,yy} + A^*_{22,xx} - A^*_{26,xy}) \tag{39c}$$

Equation (35) is transformed into a linear system of N_c equations in $N_c + M \times N$ variables by using a Galerkin technique. This is done by prioritizing the stress function: that is, by multiplying each side of the equation by the compatibility eigenfunction η_k and enforcing the *zero component of error* condition on each of the functions. The final set of equations in compact form is

$$\bar{\boldsymbol{L}}_\xi\boldsymbol{\xi} + \bar{\boldsymbol{L}}_w\boldsymbol{w} = \bar{\boldsymbol{L}}_\Delta + \bar{\boldsymbol{L}}_x N_{x0,l} + \bar{\boldsymbol{L}}_{xy}N_{xy0} + \bar{\boldsymbol{L}}_y N_{y0} \tag{40}$$

The components of matrices $\bar{\boldsymbol{L}}_\xi$ and $\bar{\boldsymbol{L}}_w$ and vectors $\bar{\boldsymbol{L}}_\Delta$, $\bar{\boldsymbol{L}}_x$, $\bar{\boldsymbol{L}}_{xy}$, and $\bar{\boldsymbol{L}}_y$ are

$$(\bar{\boldsymbol{L}}_\xi)_{ij} = \int_0^{ly}\int_0^{lx} \eta_i L_{\xi j}\,\mathrm{d}x\,\mathrm{d}y \tag{41a}$$

$$(\bar{\boldsymbol{L}}_w)_{ij} = \int_0^{ly}\int_0^{lx} \eta_i L_{wj}\,\mathrm{d}x\,\mathrm{d}y \tag{41b}$$

$$\bar{\boldsymbol{L}}_{\Delta_j} = \int_0^{ly}\int_0^{lx} \eta_j L_x\,\mathrm{d}x\,\mathrm{d}y \tag{42a}$$

$$\bar{\boldsymbol{L}}_{x_j} = \int_0^{ly}\int_0^{lx} \eta_j L_x\,\mathrm{d}x\,\mathrm{d}y \tag{42b}$$

$$\bar{\boldsymbol{L}}_{xy_j} = \int_0^{ly}\int_0^{lx} \eta_j L_{xy}\,\mathrm{d}x\,\mathrm{d}y \tag{42c}$$

$$\bar{\boldsymbol{L}}_{y_j} = \int_0^{ly}\int_0^{lx} \eta_j L_y\,\mathrm{d}x\,\mathrm{d}y \tag{42d}$$

$$\begin{aligned} &\int_0^{ly}\int_0^{lx}\left[\sum_{j=1}^{M\times N}\sum_{k=1}^{M\times N}(\varphi_{k_{,xy}}\varphi_{j_{,xy}} - \varphi_{k_{,xx}}\varphi_{j_{,yy}})w_k w_j\right]\mathrm{d}x\,\mathrm{d}y \\ &\quad \cong \int_0^{ly}\int_0^{lx}(w^2_{,xy} - w_{,xx}w_{,yy})\,\mathrm{d}x\,\mathrm{d}y = 0 \end{aligned} \tag{42e}$$

Notably, the nonlinear term involving the double summation in Eq. (35) vanishes in Eq. (40). Weaver and Nemeth [16] demonstrated that integrating over the entire domain [Eq. (42e)] and under the assumption that all the panel edges belong to the same plane, the double summation vanishes. As a result, the compatibility equation expressed in discrete compact form by Eq. (40) is a linear equation in $\boldsymbol{w}$ and $\boldsymbol{\xi}$. To solve the discretized compatibility equation, the first consideration is that the perturbation stress function ($\Delta\Psi$), the natural boundary conditions (N_{xy0}, N_{y0}), and the axial load boundary condition on the edge $x = 0$ ($N_{x0,l}$) act as load terms in Eq. (40). The second consideration is that the vector $\bar{\boldsymbol{L}}_w\boldsymbol{w}$ is null or negligible in the following two cases: 1) symmetric configurations and 2) very small transverse displacements.

In reality, symmetric configurations are rarely achieved, due to the local unsymmetric nature of the stiffener upon skin. For unsymmetric, the components B_{ij} of the coupling stiffness matrix could be large. Hence, the product $\bar{\boldsymbol{L}}_w\boldsymbol{w}$ might be sufficiently large to affect the in-plane load distribution, even in the linear regime. This effect could be more significant for thin configurations, such as skin/stringer assemblies employed in vertical and horizontal tail planes, in which the eccentricity due to the stiffeners enforces a transverse displacement field that is prominent in unbuckled configurations. This study aims at quantifying this effect in terms of actual deformed configuration and buckling loads. If only in-plane loads of small magnitude are acting, the term $\bar{\boldsymbol{L}}_w\boldsymbol{w}$ becomes negligible, and the laminate's structural response can be approximated with the symmetric model in which the total stress function Ω is well approximated by the equilibrium stress function ψ_ε [10]. Hence, by approximating the in-plane stress field with the equilibrium stress function and substituting Eqs. (11a), (11b), and (28) in Eq. (5) and performing the differentiations, a linear system of $M \times N$ equations in the $M \times N$ variables w_j is obtained:

$$(\boldsymbol{G} + \boldsymbol{H})\boldsymbol{W} = -\bar{\boldsymbol{H}}\boldsymbol{e} + \boldsymbol{Q} \tag{43}$$

where

$$\boldsymbol{G}_{ij} = \frac{1}{2}\int_0^{l_x}\int_0^{l_y}[2D_{11}^*\varphi_{,xx,i}\,\varphi_{,xx,j} + 2D_{22}^*\varphi_{,yy,i}\,\varphi_{,yy,j} + 8D_{66}^*\varphi_{,xy,i}\,\varphi_{,xy,j} + 2D_{12}^*(\varphi_{,xx,i}\,\varphi_{,yy,j} + \varphi_{,xx,j}\,\varphi_{,yy,i}) + 4D_{16}^*(\varphi_{,xx,i}\,\varphi_{,xy,j} + \varphi_{,xx,j}\,\phi_{,xy,i}) + 4D_{26}^*(\varphi_{,yy,i}\,\varphi_{,xy,j} + \varphi_{,yy,j}\,\varphi_{,xy,i})]\,\mathrm{d}x\,\mathrm{d}y \tag{44}$$

$$\boldsymbol{H}_{ij} = \int_0^{l_x}\int_0^{l_y}[\Omega_{,yy}\varphi_{,x,i}\,\varphi_{,x,j} + \Omega_{,yy}\varphi_{,y,i}\,\varphi_{,y,j} - \Omega_{,xy}(\varphi_{,x,i}\,\varphi_{,y,j} + \varphi_{,x,j}\,\varphi_{,y,i})]\,\mathrm{d}x\,\mathrm{d}y \tag{45}$$

$$\bar{\boldsymbol{H}}_{ij} = \int_0^{l_x}\int_0^{l_y}[\Omega_{,yy}\varphi_{,x,i}\,\bar{\varphi}_{,x,j} + \Omega_{,yy}\varphi_{,y,i}\,\bar{\varphi}_{,y,j} - \Omega_{,xy}(\varphi_{,x,i}\,\bar{\varphi}_{,y,j} + \bar{\varphi}_{,x,j}\,\varphi_{,y,i})]\,\mathrm{d}x\,\mathrm{d}y \tag{46}$$

and $\Omega = \Psi_e$.

Equation (43) can be inverted to yield an approximate expression for the transverse displacement. The induced error is assumed negligible when the external loading is insignificant if compared with the critical buckling level for the same loading condition:

$$\boldsymbol{W} = -(\boldsymbol{G} + \boldsymbol{H})^{-1}\bar{\boldsymbol{H}}\boldsymbol{e} \tag{47}$$

Once the transverse displacement is known in terms of the coefficients of its generalized Fourier series expansion, Eq. (40) can be inverted giving the approximate expression of the total in-plane stress function:

$$\boldsymbol{\xi} = (\bar{\boldsymbol{L}}_\xi)^{-1}[\bar{\boldsymbol{L}}_w(\boldsymbol{G} + \boldsymbol{H})^{-1}\bar{\boldsymbol{H}}\boldsymbol{e} + \bar{\boldsymbol{L}}_\Delta + \bar{\boldsymbol{L}}_x N_{x0,l} + \bar{\boldsymbol{L}}_{xy}N_{xy0} + \bar{\boldsymbol{L}}_y N_{y0}] \tag{48}$$

Equation (48) represents the generalized amplitudes for the Fourier representation of Ψ_c. The updated value of Ω is calculated and substituted into Eq. (47) to obtain an updated value of w. Then successive calculations of Ω via Eq. (47) and w are done until converged solutions are reached. Note that if the external in-plane loads are comparable with their critical buckling level, then the step-by-step approach just outlined must be employed to update the in-plane stress field at the beginning of each step and to allow a more accurate calculation of the actual transverse displacements.

Let

$$\bar{\boldsymbol{N}}_0 = \begin{bmatrix} \bar{N}_{x0,l} \\ \bar{N}_{y0} \\ \bar{N}_{xy0} \end{bmatrix} \tag{49a}$$

$$\bar{\boldsymbol{N}}_{0,cr} = \bar{\lambda}_{cr}\begin{bmatrix} \bar{N}_{x0,l} \\ \bar{N}_{y0} \\ \bar{N}_{xy0} \end{bmatrix} \tag{49b}$$

represent the acting load and the critical buckling load level, respectively. The load path is discretized in a finite number N_P of load steps $\Delta\bar{\boldsymbol{N}}_{0k} = \bar{\boldsymbol{N}}_0/N_P + 1$, from the unloaded base state ($k = 0$) to the actual load level $\bar{\mathbf{N}}_0$ ($k = N_P$):

$$\bar{\boldsymbol{N}}_{0_k} = \frac{k}{N_P}\bar{\boldsymbol{N}}_0 \tag{50}$$

The subscript k is used to represent the generic variable calculated at the kth step. The following algorithm is used for the approximate calculation of the transverse displacement and the in-plane stress function at each step k:

$$\boldsymbol{W}_k = -(\boldsymbol{G} + \boldsymbol{H}(\Psi_{e_k} + \Psi_{c_{k-1}}))\bar{\boldsymbol{H}}(\Psi_{e_k} + \Psi_{c_{k-1}})\boldsymbol{e} \tag{51a}$$

$$\boldsymbol{\xi}_k = (\bar{\boldsymbol{L}}_\xi)^{-1}\{\bar{\boldsymbol{L}}_w[\boldsymbol{G} + \boldsymbol{H}(\Psi_{e_k} + \Psi_{c_{k-1}})]^{-1}\bar{\boldsymbol{H}}(\Psi_{e_k} + \Psi_{c_{k-1}})\boldsymbol{e} + \bar{\boldsymbol{L}}_{\Delta k} + \bar{\boldsymbol{L}}_x N_{x0,l_k} + \bar{\boldsymbol{L}}_{xy}N_{xy0_k} + \bar{\boldsymbol{L}}_y N_{y0_k}\} \tag{51b}$$

For each step, the proposed algorithm replaces the actual value of the compatibility stress function with the value taken at the end of the previous step.

It is emphasized that because the actual transverse displacement's magnitude and shape affects the in-plane stress function, a sensitivity of the in-plane stress distribution to the essential boundary conditions for the transverse displacement is expected. Let us consider, for example, two identical unsymmetrically laminated panels loaded by the same system of in-plane loads, but with different kinematical boundary conditions. It is realistic to expect the behavior of the panel subjected to more restrictive (in terms of transverse displacements) boundary conditions to be reasonably approximated by the symmetric model because the effect of the coupling matrix $\boldsymbol{B}$ is minimized.

V. Model Validation and Buckling Singularities

A composite assembled panel (Fig. 7a), consisting of a square skin and a rectangular reinforcement (patch), was analyzed to compare this analysis with the symmetric model proposed by Cosentino and Weaver [10] and to assess the differences and their causes. Furthermore, both models were compared with FEM.

The in-plane stress field calculated by means of the proposed analytical solution was first compared with FEM. In-plane normal forces arising along the sections indicated in Fig. 7b were compared. The finite element simulations were done using ABAQUS commercial software. The domain was discretized by means of quadratic quadrilateral elements S8R [17]. Each square has a 2 mm edge length (Fig. 8).

An offset was assigned to all the elements that represent the skin-reinforcement overlap region. The offset equals the difference of the two $x$wise neutral planes, overlap and skin regions, respectively. Material properties and geometrical parameters are reported in Tables 1 and 2, respectively. Stacking sequences are reported in Table 3.

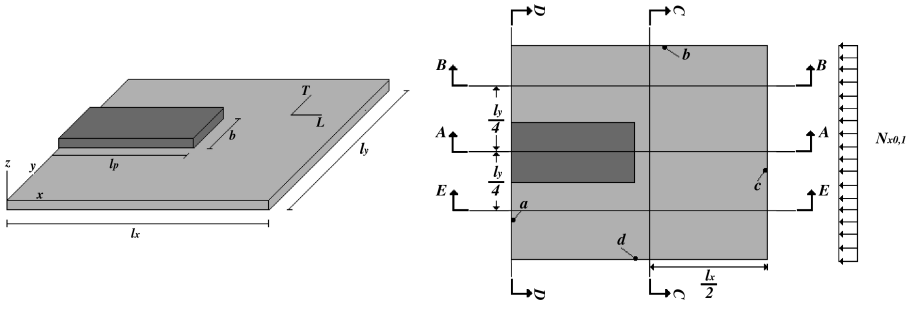

a) b)

Fig. 7 Reinforced panel: a) geometry and b) plant view.

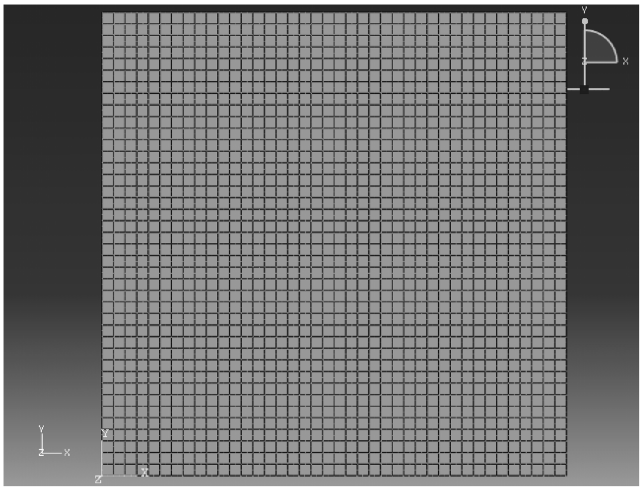

Fig. 8 Finite element model mesh detail.

The enforced boundary conditions consist of simple supports along all of the edges. Functions (31) were employed to model the compatibility stress function Ψ_c. The following functions were used to expand the eccentricity e and the components A^*_{ij} and B^*_{ij} of the matrices of in-plane flexibility and coupling, respectively [5]:

$$\bar{X}_i = 1 - \cos\left(\frac{i\pi(l_x - x)}{2l_x}\right) \tag{52a}$$

$$\bar{Y}_j = \sin\left(\frac{j\pi y}{l_y}\right) \tag{52b}$$

A total of 10 eigenfunctions were employed for each coordinate. Similarly, a total of 10 functions were used to calculate and express the perturbation stress function $\Delta\Psi$ by means of Eq. (23). A crosswise product superposition of eigenfunctions (10 per each coordinate) of simply supported beams were used to expand the transverse displacement w:

$$X_i = \sin\left(\frac{i\pi x}{l_x}\right) \tag{53a}$$

$$Y_j = \sin\left(\frac{j\pi y}{l_y}\right) \tag{53b}$$

Table 1 Lamina properties

Component	E_L, MPa	E_T, MPa	G_{LT}, MPa	ν_{LT}	Thickness, mm
Patch	150,000	8,800	4,800	0.35	0.2
Skin	150,000	8,800	4,800	0.35	0.2

Table 2 Geometrical parameters

Parameter	Value
l_x, mm	100
l_y, mm	100
l_p, mm	50
b, mm	20

Table 3 Stacking sequences

Configuration	Component	Stacking sequence
1	Patch	$[45/-45]$
2	Skin	$[0/90]$

A total of 20 load increments were used to solve Eqs. (51a) and (51b).

The structural response to the applied compressive axial load $N_{xo,l}$ (Fig. 7b) was simulated. Two different cases were analyzed. In the first simulation, the two opposite unloaded edges b and d (Fig. 7b) were free to move in the y direction and did not restrain the shear deformation induced by the nonnullity of A^*_{16}. As a result, the in-plane stress field was mainly dominated by the axial compression. An axial load $N_{xo,L} = -0.58$ N/mm was applied. The transverse displacements predicted by this analysis are reported in Fig. 9a. Figure 9b shows the transverse displacements predicted by the simplified symmetric model.

As shown, this analysis predicts larger transverse displacements when compared with predictions obtained from the symmetric model. The predicted deformed shapes are very similar in both cases. To assess the predicted quasi-nonlinear behavior and quantify the effect of asymmetry, the maximum amplitudes of predicted transverse displacements are plotted against the external load and compared in Fig. 10.

As expected, the error induced by using the simplified symmetric model is negligible when the external loading is insignificant compared with the critical buckling level for the same loading condition. When the load becomes larger and comparable to the buckling load, the effect of the transverse displacement becomes significant in the compatibility Eq. (51b). In-plane load redistributions are predicted, which cause the compatibility stress function Ψ_c to be comparable in magnitude to the equilibrium stress function Ψ_e, thus influencing the calculation of the $\boldsymbol{H}$ and $\bar{\boldsymbol{H}}$ matrices. Hence, the calculated transverse displacements begin to diverge. The in-plane load $N_{x,e}$ calculated by means of the equilibrium stress function (equal for both symmetric and unsymmetric models), and the additional $N_{x,c}$ calculated by means of the compatibility stress function, were calculated at the actual load level. Results are reported in Fig. 11.

As shown in Figs. 11b and 11c, there is noteworthy in-plane loads redistribution triggered by the transverse displacements. The difference between the two approaches becomes appreciable as soon as the actual applied in-plane loads approach their critical values.

Two considerations are necessary:

1) When the external loading system is sufficiently close to its critical magnitude, Eq. (43) cannot be straightforwardly inverted as the determinants of both the $\boldsymbol{G}$ and $\boldsymbol{H}$ matrices are close to zero. The reason is implicit in the mathematical definition of buckling. The critical loading condition causes a simultaneous diagonalization of both matrices; resulting in an important decrease of accuracy, and reliability of both models cannot be avoided.

2) If the maximum absolute value of the transverse displacement $w_{\max}$ reaches the threshold beyond which the linear approaches become inadequate, a fully nonlinear approach is required to obtain accurate structural responses. This threshold is generally expressed in terms of the ratio between transverse displacement and skin thickness. Typically, the beginning of geometrically nonlinear regimes is defined for values of this ratio that exceed 0.1–0.2 [18].

For illustrative purposes, a second analysis was undertaken on the same configuration and enforcing the same boundary conditions. The external in-plane load $N_{xo,L}$ was set to -1.5 N/mm. The maximum amplitudes of predicted transverse displacements are plotted against the external load and compared in Fig. 12.

As shown in Fig. 12, there are peaks which correspond to buckling onsets. In the proximity of the first peak, and for all loads exceeding this value, the approximate nonlinear model is no longer suitable to solve the analyzed problem. The same analysis was carried out by imposing a tensile external load of the same magnitude. The maximum amplitudes of predicted transverse displacements are plotted against the external load and compared in Fig. 13.

As evident, the difference between the two models increases with the transverse displacement, but at a much smaller rate. The effect of tensile loads is, in fact, a notable reduction of the transverse displacements induced by the eccentricity. As a consequence, both models supply similar responses and their range of validity is notably widened.

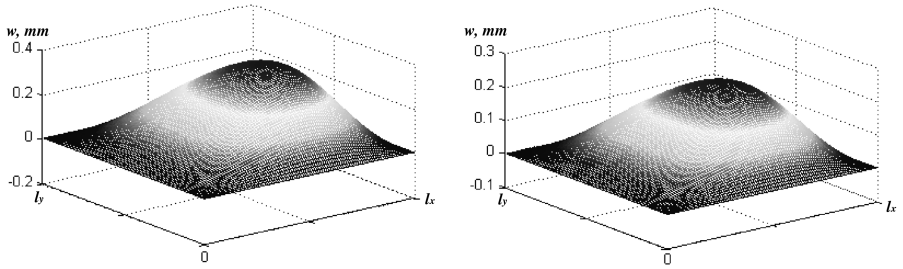

Fig. 9 Transverse displacement: a) present analysis and b) symmetric model.

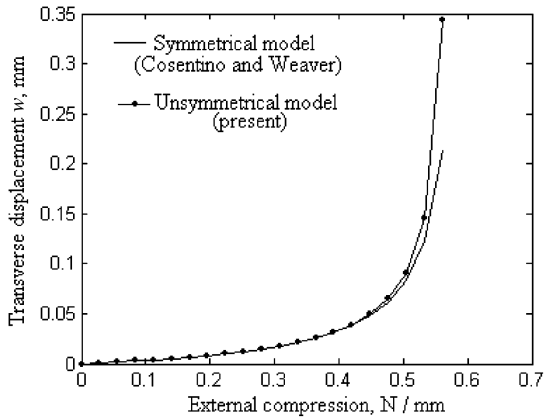

Fig. 10 Compared maximum transverse displacements.

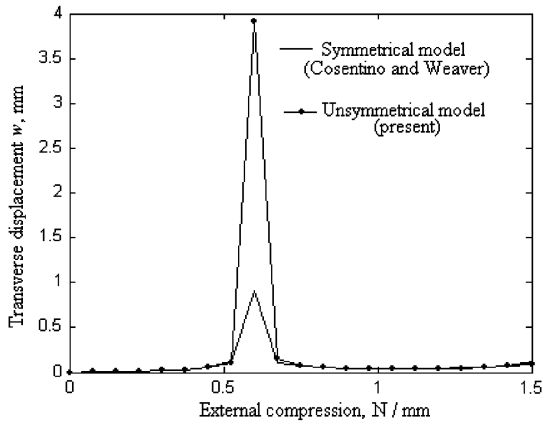

Fig. 12 Compared maximum transverse displacements for in-plane loading exceeding the critical buckling load.

In a second simulation, the *y*wise displacements of the two opposite unloaded edges *b* and *d* (Fig. 7b) were restrained in addition to the shear deformation induced by the nonnullity of A_{16}^{*}. As a result, no predominant direction can be specified for the in-plane stress field. A compressive axial load $N_{xo,L} = -1.5$ N/mm was applied. The maximum amplitudes of predicted transverse displacements are plotted against the magnitude of the external load and compared in Fig. 14.

The responses of both models are reasonably similar in the linear regime and begin to diverge as the transverse displacements become significantly large compared with the skin thickness. Once again, the reasons for the divergent responses lie in the in-plane loads redistribution due to the asymmetry. For small displacements, the component of in-plane loads due to the compatibility stress function is negligible compared with the equilibrium components; that is, the in-plane stress field is dominated by the load term represented by the natural boundary conditions [refer to Eq. (51b)]. As the external loads increase in magnitude, the equilibrium load term increases linearly, as shown by Eq. (35), while the effect of the transverse displacement increases at a larger rate. In fact, compressive loads exacerbate the internal bending due to transverse displacement, triggering a magnifying effect on the displacements magnitude. This phenomenon is diminished in the case of tensile external loads.

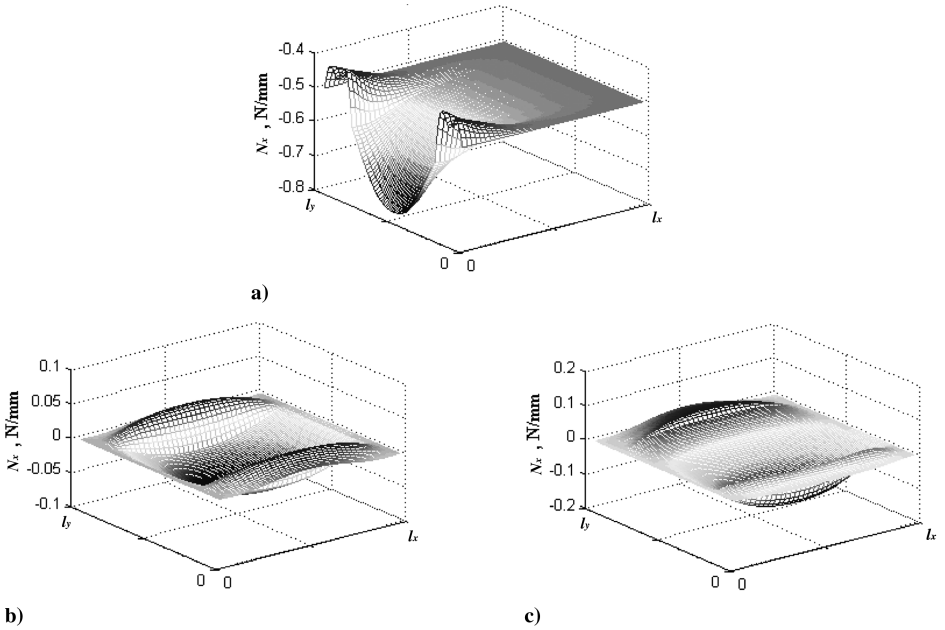

Fig. 11 Example of internal in-plane axial loads: a) equilibrium component, b) compatibility component for the symmetric model, and c) compatibility component for the unsymmetric model.

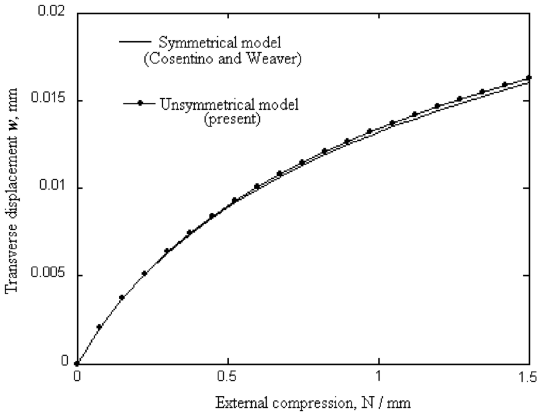

Fig. 13 Compared maximum transverse displacements for in-plane tensile loading.

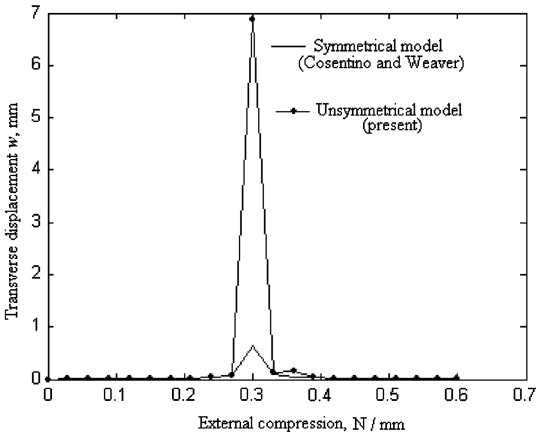

Fig. 14 Compared maximum transverse displacements for in-plane loading exceeding the critical buckling load.

The predicted peaks give no information about the structural response but show that panel buckling onset is located in the region of load magnitude that is underneath the displacement peak. As predicted, the peaks show a discernible reduction of buckling load due to biaxial compression being triggered by restraining the Poisson's transverse (*y*wise) expansion of the panel.

As the in-plane load increases in magnitude, internal in-plane load redistributions occur. To confirm this behavior, the in-plane longitudinal stress resultants N_x were calculated at two different load magnitudes using both models. The critical buckling load calculated by means of the symmetric model was used as the reference load. Results are illustrated and compared in Figs. 15–17.

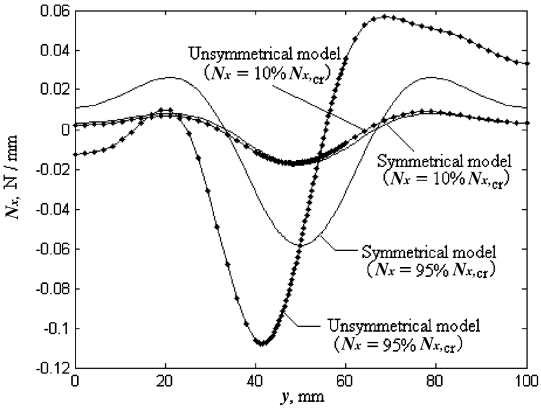

Fig. 15 Compatibility components of axial in-plane stress resultant for section CC (midbay).

Both models predict reasonably similar distributions when the external load level is small compared with the buckling load. As the external load increases, clear evidence of load redistribution is predicted by this analysis. It is noteworthy to observe that not only the deformed shapes of unsymmetrically laminated panels are skewed in appearance; this behavior also extends to the shape of in-plane loads distributions. This effect is clearly noticeable in Fig. 17 in which the spanwise distributions of longitudinal stress resultants are plotted along two sections [namely, BB and EE (refer to Fig. 7)], which are symmetrically located with respect to the panel's longitudinal axis of symmetry. Load redistributions are notable from small values of the external load and become more significant as the load increases in magnitude.

VI. Sensitivity Analysis and Buckling Calculation Procedure

Results obtained in the previous section suggest that considerable in-plane loads redistribution might occur during the prebuckling regime. In the aerospace industry, for sizing purposes, the effect of transverse displacements on the buckling calculation is sometimes taken into account by introduction of semi-empirical knockdown factors used to adjust the linear analysis. Let us consider, for example, a symmetrically laminated flat composite panel preloaded by transverse pressure and then undergoing uniaxial compressive load. If the magnitude of pressure is sufficiently large to trigger significant transverse displacements (for instance, in thin-sectioned panels), but not enough to cause important membrane stretching, then the buckling loads calculated with and without considering the pressurization phase are identical. The effect of the pressure is comparable to an initial perturbation and the classical two-dimensional Euler's formulation remains valid. In the linear regime, as the external load increases in magnitude, the in-plane stresses distribution typically varies in a self-similar manner. Hence, the calculation of buckling loads does not depend on the actual level of the external loads. In contrast, Eq. (10) and Figs. 15–17 reveal that in-plane stress redistribution takes place in unsymmetric configurations such as stringer terminations undergoing relatively large transverse displacements, and are coupled with the in-plane loading due to the eccentricity of the neutral plane. As the magnitude of the external loads increase, such configurations exhibit in-plane stress distributions that vary in a manner that is not self-similar. Therefore, the calculation of buckling loads can be significantly affected by the actual maximum load level input to compute the iterations (51a) and (51b) and solve the eigenvalue problem. Equations (49a) and (49b) suggest that the calculation of buckling loads becomes more and more accurate as the actual external load $\bar{\boldsymbol{N}}_0$ approaches the critical load $\bar{\boldsymbol{N}}_{0,\mathrm{cr}}$. Furthermore, results shown in Figs. 12 and 14 show that when the actual load exceeds the buckling load, numerical instabilities are generated when solving the eigenvalue problem. Therefore, to obtain reliable results, the value of the maximum external load input and used to calculate buckling loads must tend to the critical load from the left:

$$\bar{\boldsymbol{N}}_0 \leq \bar{\boldsymbol{N}}_{0,\mathrm{cr}} \tag{54}$$

The closer the actual load to the critical value, the more accurate the linear calculation of buckling loads, based on the eigenvalue problem applied to Eq. (47).

Therefore, the use of an initial guess, which is as large as possible, is generally recommended to improve the effectivity of the proposed analysis. However, there is an additional constraint due to the limits of applicability of the this model. In fact, if the maximum value of the nondimensional ratio w/t_s (where w is the transverse displacement and t_s is the skin thickness) exceeds the threshold value that typically delimits the linear from the nonlinear regime, then the validity of the results obtained by means of this approach might be rather inaccurate and a fully nonlinear approach would be required. The value of 0.2 [18] was chosen for the aforementioned threshold value as the break point for the calculation subroutine used to validate this model.

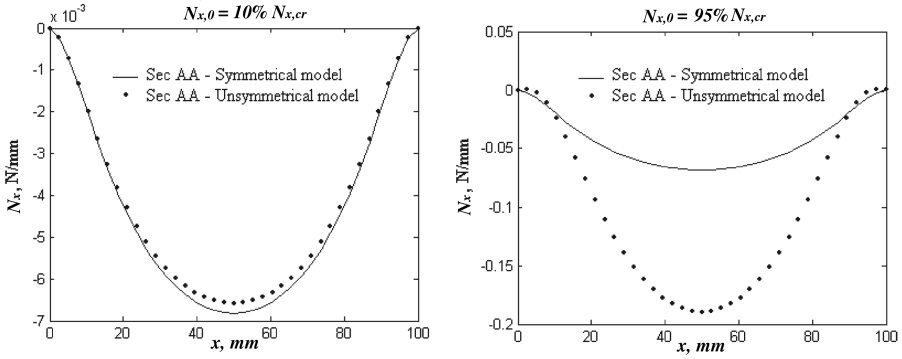

a) b)

Fig. 16 Compatibility components of axial in-plane stress resultant for section (Sec) AA.

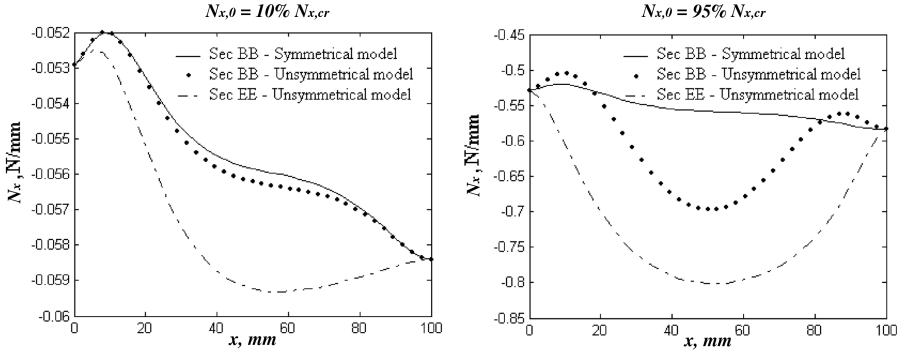

a) b)

Fig. 17 Axial in-plane stress resultant for sections BB and EE.

Two main parameters are recognized to affect the degree of accuracy of this analysis 1) the magnitude of the initial guess $\bar{\mathbf{N}}_0$, and 2) the total number of load increments $\bar{\mathbf{N}}_{0_k}$.

With regard to the first parameter, the approach employed is described in the following steps:

1) The buckling load calculated by means of the symmetric model is used as a first guess.

2) The interval $[0, \bar{\mathbf{N}}_0]$ is divided into a number N_P of equal steps, each of them representing the discrete load increments $\bar{\mathbf{N}}_{0_k}$ defined in Eq. (50).

3) Iterations (51a) and (51b) are performed until one of the following conditions is reached: a) $w_{\max}/t_s = 0.2$ or b) $k \times \bar{N}_{0_k} = 0.95 \times \bar{N}_{0,\mathrm{cr}_k}$, where $\bar{\mathbf{N}}_{0,\mathrm{cr}_k}$ is the critical buckling load calculated using the actual load distribution at the end of each step.

4) If none of the preceding conditions are verified, the initial guess is incremented by the nominal load increment $\bar{\mathbf{N}}_{0k}$.

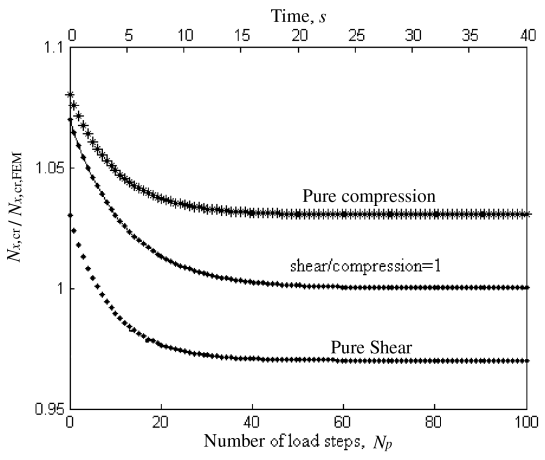

Fig. 18 Compared buckling loads and sensitivity analysis.

5) Iterations 1–4 are performed until either the magnitude of the initial guess $\bar{\mathbf{N}}_0$ or the total number of load increments $\bar{\mathbf{N}}_{0_k}$ is reached.

With regard to the total number of steps used to discretize the load interval, a sensitivity study was undertaken to assess this effect and to choose a suitable number of load steps, which guarantees the best compromise of accuracy and calculation time. The buckling loads of the reinforced panel illustrated in Sec. V were calculated and compared with a nonlinear FEM calculation for three different load cases. Results are reported in Fig. 18.

Although the total number of steps required to achieve convergence appears large, after 30 steps the convergence slope is sufficiently small to consider that the algorithm has converged. Computational times are reported in the axis located on top of Fig. 18. It is noted that an average time that is between 10 and 15 s is required to complete the full analysis. This study was, of course, limited to the case of the panel studied in Sec. V and further sensitivity analyses would be required to thoroughly investigate the numerical behavior for a variety of configurations and kinematical boundary conditions. However, this is beyond the scope of the present study. The aim of the sensitivity analysis performed was to set a number of steps to perform reliable buckling analyses and subsequent comparisons with FEM.

VII. Buckling Interaction Curves

Buckling interaction curves were derived for a variety of cases using both the symmetric and the unsymmetric models. Results were compared with FEM. In the first batch of analyses, the interaction curves were obtained for the panel analyzed in Sec. VI. Two different sets of boundary conditions were considered. The sets include all edges simply supported and all edges built in, respectively. Results are reported in Figs. 19a and 19b. In addition, buckling interaction curves are calculated for a typical aerospace composite wing assembly consisting of a T-sectioned composite stringer and a skin. The panel is illustrated in Fig. 20. The same lamina properties were assumed for both assemblies and details can be found in Table 1. Geometry and stacking sequences are reported in Tables 4 and 5,

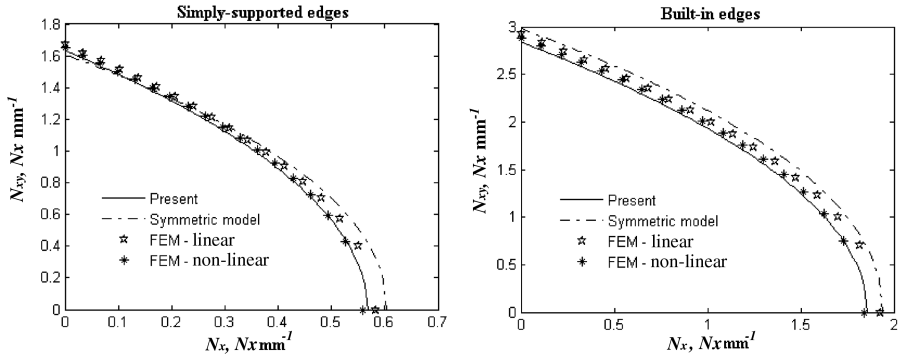

Fig. 19 Interaction curves for skin/patch-type panel.

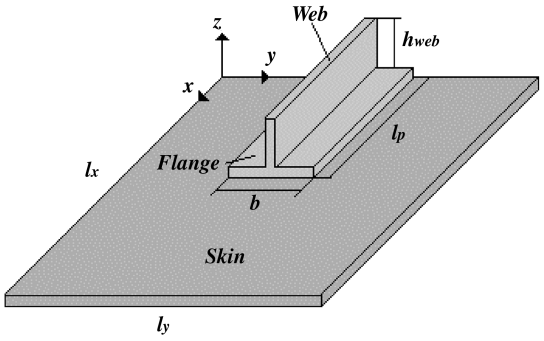

Fig. 20 Stiffened composite panel.

respectively. Comparisons with FEM are illustrated in Figs. 21a and 21b.

It is noteworthy that the effect of asymmetry is, in the examined cases, unfavorable. If taken into account by means of more accurate models in conjunction with fully (FEM) or approximate (this analysis) nonlinear calculations, the calculation of buckling loads results in a considerable reduction, especially when the axial compression is the main component of the external loading.

Notably, two FEM analyses (namely, linear and nonlinear) were done to assess the effect of load redistribution. In the linear case, a small axial load was input and buckling loads were calculated using the linear perturbation buckling calculation [17]. For the nonlinear calculation, two steps were defined that replicate the analytical strategy. A first nonlinear step was defined in which the external load was set to a value equal to 80% of the linear buckling load calculated previously by means of the linear perturbation method. Then, linear buckling analyses were performed on the actual deformed configuration. It is noted that the calculation time needed to derive each point on the interaction curves is between 100 and 120 s with FEM. When compared with 15 to 20 s required by this model, it justifies the choice of the proposed analytical approach. Furthermore, it must be highlighted that the calculation times do not take into account the model setup, which is the most expensive phase in terms of time for the FEM. This approach was implemented in a fully parametric tool that required negligible setup time, thus increasing the associated advantages.

Figures 19 and 21 show that the effect of load redistribution is captured by FEM and significantly affects the buckling loads. Also, both the analytical approach and the FEM predict differences between the linear and nonlinear approaches that increase as the shear/compression ratio tends to zero (i.e., pure axial compression). Therefore, the perturbation introduced by the stiffener significantly affects the axial in-plane load distribution, but it produces minor effects on in-plane load redistribution when the panel is loaded in shear. Furthermore, as expected, the disagreement of both predictions is larger in the simply supported case than in the case in which all the edges are built in. The latter boundary condition is more restrictive in terms of induced transverse displacements; therefore, the effect of the coupling stiffness matrix $\boldsymbol{B}$ is, to a certain extent, reduced as predicted by the compatibility equation. The degree of asymmetry was particularly exacerbated in the skin/patch-type panel for illustrative purposes. Of course, stacking sequences and geometry chosen are not representative of typical aerospace structures. In contrast, the composite assembly illustrated in Fig. 20 can be considered as an example of real substructure. Although made of a symmetric skin, the structural behavior of such a structure is influenced by the geometrical asymmetry due to the presence of the stringer. Referring to Fig. 4, the skin/flange/web and the skin/flange sections are intrinsically unsymmetric. The degree of asymmetry is reduced if a tall web is used, so that the section can be idealized as web only, and the local influence of flange and skin is negligible. However, as the web height increases, the $\mathbf{B}$ matrix increases in magnitude and its effect on the global structural response can be important. Furthermore, the secondary bending introduced increases with the web height, triggering significant transverse displacements. Hence, the combined effect of the components $\mathbf{B}_{ij}$ and the transverse displacements is noteworthy. Therefore, panels with stringer run-outs exhibit structural behavior that is intrinsically unsymmetric. As such, to systematically calculate the critical buckling loads, an analytical or FEM model able to capture load redistributions by means of step-by-step procedures might be required. It is important that the procedure adopted follows the guidelines provided in Sec. VI: that is, that the actual load tends to the critical buckling load from lower values. Also, the calculation of buckling loads should be performed at the end of each step to ensure that the actual load has not exceeded the buckling load. In fact, in such a case, the linear calculation would be effected by different load redistributions that are triggered in the unstable regime, but are not present within the stable regime. A nonlinear buckling calculation is recommended and should be preferred to other methods, such as bifurcation analyses. As shown in this study, in highly eccentric configurations, the

Table 4 Geometrical parameters

Parameter	Value
l_x, mm	200
l_y, mm	100
l_P, mm	50
h_{web}, mm	30
b, mm	20

Table 5 Stacking sequences

Component	Stacking sequence
Web	$[0/90/0/0/-45/0/45/0/45/0/-45]_S$
Flange	$[0/90/0/0/-45/0/45/0/45/0/-45]$
Skin	$[0/45/0/-45/90/0]_S$

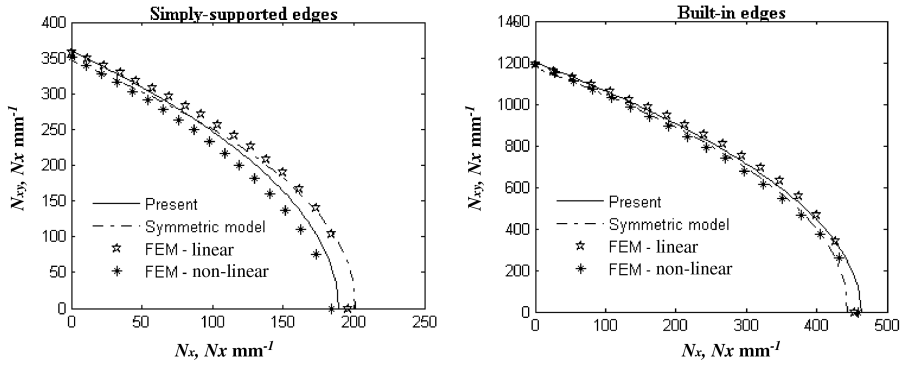

Fig. 21 Interaction curves for stiffened composite assembly.

transverse displacements can be significant, even during the prebuckling loading phase. Snap-through phenomena and sudden bending, on which the bifurcation analyses are based, may not take place. Therefore, it is extremely difficult to estimate buckling loads if the transition from stable to unstable regimes is smooth.

Finally, it is noteworthy that satisfying equilibrium appears more important than satisfying compatibility. Figures 11 and 15–17, show that in the stable regime and for loads approaching the buckling level, the average ratio between compatibility stress function ψ_c and the equilibrium stress function ψ_e is between $1/10$ and $1/5$. The same ratio is observed between the maximum transverse displacement and the skin thickness. As a preliminary conclusion, the compatibility component to the overall stress function Ω can be considered as a perturbation when the transverse displacements do not exceed a threshold delimiting the linear and the nonlinear regimes. Additional studies are required to further assess the effect of satisfying compatibility in highly nonlinear regimes, such as those occurring in postbuckled structures.

VIII. Conclusions

A hybrid meshless approach was developed and used to predict prebuckling and buckling of discretely assembled multibay composite panels made from skin and stiffeners. Numerical results obtained were compared with FEM and show very good correlation in terms of in-plane loads distribution and buckling loads calculation. The effect of eccentricity on the calculation of buckling loads was highlighted in the case of this analysis and for analyses done with FEM. A strong link between nonlinearity and eccentric/unsymmetric configuration was substantiated. The intrinsic limitations of the proposed approach were discussed. However, a thorough deployment of this approach or the FEM procedure proposed hereby could require further tuning and calibration studies that were beyond the scope of this study. For example, the tolerances could be modified to fit with available experimental data. The main aim of this paper was to highlight and quantify discrepancies that could arise when simple models are used to simulate more complex configurations, such as composite panels with stringer terminations, and to propose a fast method for preliminary (but careful) structural assessments.

Acknowledgment

The authors would like to thank Airbus, Ltd., for the financial support provided.

References

[1] Williams, J. G., "On the Calculation of Energy Release Rates for Cracked Laminates," *International Journal of Fracture*, Vol. 36, No. 2, 1988, pp. 101–119.
doi:10.1007/BF00017790

[2] Stevens, K. A., Ricci, R., and Davies, G. A., "Buckling and Post-Buckling of Composite Structures," *Composites*, Vol. 26, No. 3, 1995, pp. 189–199.
doi:10.1016/0010-4361(95)91382-F

[3] Dahlen, C., and Springer, G. S., "Delamination Growth in Composites Under Cyclic Loads," *Journal of Composite Materials*, Vol. 28, No. 8, 1994, pp. 732–781.

[4] Falzon, B. J., and Davies, G. A. O., "The Behavior of Compressively Loaded Stiffener Runout Specimens—Part 2: Finite Element Analysis," *Journal of Composite Materials*, Vol. 37, No. 6, 2003, pp. 481–501.
doi:10.1177/0021998303037006416

[5] Cosentino, E., and Weaver, P. M., "A Non-Linear Analytical Approach for Sizing of Discrete Composite Stringer Terminations," *AIAA Journal*, Vol. 47, No. 3, Mar. 2009, pp. 606–617.
doi: 10.2514/1.37745

[6] Falzon, B. J., and Davies, G. A. O., "The Behavior of Compressively Loaded Stiffener Runout Specimens—Part 1: Experiments," *Journal of Composite Materials*, Vol. 37, No. 5, 2003, pp. 381–400.
doi:10.1177/0021998303037005407

[7] Meeks, C., Greenhalgh, E., and Falzon, B., "Stiffener Debonding Mechanism in Post-Buckled CFRP Aerospace Panels," *Composites*, Pt. A, Vol. 36, 2005, pp. 934–946.
doi:10.1016/j.compositesa.2004.12.003

[8] Cosentino, E., and Weaver, P. M., "Approximate Non-Linear Analysis Method for Debonding of Skin/Stringer Composite Assemblies," *AIAA Journal*, Vol. 46, No. 5, 2008, pp. 1144–1159.
doi: 10.2514/1.31914

[9] Mittelstedt, C., "Closed-Form Analysis of the Buckling Loads of Uniaxially Loaded Blade-Stringer-Stiffened Composite Plates Considering Periodic Boundary Conditions," *Thin-Walled Structures*, No. 45, 2007, pp. 371–382.

[10] Cosentino, E., and Weaver, P. M., "Buckling of Stiffened Composite Panels with Stringer Terminations," *International Journal of Mechanics of Materials and Solids* (submitted for publication).

[11] Weaver, P. M., "Approximate Analysis for Buckling of Compression Loaded Long Rectangular Plates with Flexural/Twist Anisotropy," *Proceedings of the Royal Society of London, Series A: Mathematical and Physical Sciences*, Vol. 462, No. 2065, 2006, pp. 59–73.
doi:10.1098/rspa.2005.1552

[12] Reddy, J. N., *Mechanics of Laminated Composite Plates and Shells*, CRC Press, Boca Raton, FL, 2004.

[13] Ashton, J. E., Halpin, J. C., and Petit, P. H., *Primer on Composite Materials: Analysis*, Technomic, Lancaster, PA, 1969, pp. 128–131.

[14] Jaunky, N., Knight, N. F., Jr., and Ambur, D. R., "Buckling of Arbitrary Quadrilateral Anisotropic Plates," *AIAA Journal*, Vol. 33, No. 5, 1995, pp. 938–944.
doi:10.2514/3.12512

[15] Timoshenko, S. P., and Goodier, J. N., *Theory of Elasticity*, 3rd ed., McGraw–Hill, New York, 1982, pp. 53–56.

[16] Weaver, P. M., and Nemeth, M. P., "Bounds on Flexural Properties and Buckling Response for Symmetrically Laminated Composite Plates," *Journal of Engineering Mechanics*, Vol. 133, No. 11, 2007, pp. 1178–1191.
doi:10.1061/(ASCE)0733-9399(2007)133:11(1178)

[17] ABAQUS, Ver. 6.5.3, User Manual, Vol. 4, ABAQUS, Ltd., London, 2004.

[18] Bruhn, E. F., *Analysis and Design of Flight Vehicle Structures*, Jacobs, Carmel, IN, 1973.

A. Palazotto
Associate Editor